PAPER • OPEN ACCESS

Two-dimensional MSi$_2$N$_4$ (M = Ge, Sn, and Pb) monolayers: promising new materials for optoelectronic applications

View the article online for updates and enhancements.

2D Materials

CrossMark

Two-dimensional $M\mathrm{Si}_2\mathrm{N}_4$ (M = Ge, Sn, and Pb) monolayers: promising new materials for optoelectronic applications

Mirali Jahangirzadeh Varjovi[1,*], **Soheil Ershadrad**[2], **Biplab Sanyal**[2] and **Sergio Tosoni**[1,*]

1   Department of Materials Science, University of Milano-Bicocca, Via Roberto Cozzi 55, 20125 Milano, Italy
2   Department of Physics and Astronomy, Uppsala University, Box-516, 75120 Uppsala, Sweden
*   Authors to whom any correspondence should be addressed.

E-mail: mirali.jahangirzadehvarjovi@unimib.it and sergio.tosoni@unimib.it

Abstract

The recent growth of two-dimensional (2D) layered crystals of $\mathrm{MoSi}_2\mathrm{N}_4$ and $\mathrm{WSi}_2\mathrm{N}_4$ has sparked significant interest due to their outstanding properties and potential applications. This development has paved the way for a new and large family of 2D materials with a general formula of MA_2Z_4. In this regard, motivated by this exciting family, we propose two structural phases (*1T*- and *1H*-) of $M\mathrm{Si}_2\mathrm{N}_4$ (M = Ge, Sn, and Pb) monolayers and investigate their structural, vibrational, mechanical, electronic and optical properties by using first-principles methods. The two phases have similar cohesive energies, while the *1T* structures are found to be more energetically favorable than their *1H* counterparts. The analysis of phonon spectra and *ab initio* molecular dynamics simulations indicate that all the suggested monolayers, except for *1H*-$\mathrm{GeSi}_2\mathrm{N}_4$, are dynamically and thermally stable even at elevated temperatures. The elastic stability and mechanical properties of the proposed crystals are examined by calculating their elastic constants (C_{ij}), in-plane stiffness ($Y_{2\mathrm{D}}$), Poisson's ratio (ν), and ultimate tensile strain (UTS). Remarkably, the considered systems exhibit prominent mechanical features such as substantial in-plane stiffness and high UTS. The calculated electronic band structures reveal that both the *1T*- and *1H*-$M\mathrm{Si}_2\mathrm{N}_4$ nanosheets are wide-band-gap semiconductors and their energy band gaps span from visible to ultraviolet region of the optical spectrum, suitable for high-performance nanoelectronic device applications. Lastly, the analysis of optical properties shows that the designed systems have isotropic optical spectra, and depending on the type of the system, robust absorption of ultraviolet and visible light (particularly in *1H*-$\mathrm{PbSi}_2\mathrm{N}_4$ monolayer) is predicted. Our study not only introduces new members to the family of 2D MA_2Z_4 crystals but also unveils their intriguing physical properties and suggests them as promising candidates for diverse nanomechanical and optoelectronic applications.

1. Introduction

In recent years, with the successful isolation of single-layer graphene [1], an intensive research interest has been attracted towards the field of two-dimensional (2D) materials [2–4]. The quest for novel ultrathin materials has led to the exploration of a wide range of 2D materials with remarkable physical properties and potential applications in advanced devices [5–8]. Within the 2D dynasty, transition metal dichalcogenides (TMDs), and transition metal nitrides (TMNs) have attracted tremendous interest in many research fields owing to their stability

and outstanding electronic properties ranging from semiconducting and metallic to superconducting [9–11]. According to the coordination configuration of constituent atoms, TMDs, and TMNs monolayers with the general formula of MX_2 can be commonly formed in the centered honeycomb (*1T*-phase, octahedral lattice), or honeycomb (*1H*-phase, trigonal prismatic coordination) structures [12, 13]. The study of the phase engineering and phase transition between various forms of TMDs and TMNs is gaining attention because the possibility of enabling distinct functionalities in the same material offers unique features and opportunities [14, 15]. Various techniques

are available to induce phase transition from the *1T* to *1H* form (or vice versa), such as applying stresses [16] and changing temperature [17]. In addition to TMDs and TMNs, a new family of 2D materials, single-layer group-IV chalcogenides, has gained considerable attention due to their stability and remarkable optoelectronic properties [18–21]. Through the chemical vapor deposition (CVD) technique, Xu *et al* synthesized ultrathin 2D SnS_2 crystals, which have been utilized as field effect transistors (FETs) [22]. Following that, a theoretical study has shown that SnS_2 nanosheet can be dynamically stable in both *T*- and *H*- phases [23]. Furthermore, a series of group IV dichalcogenide monolayers, *MXY* ($M =$ Ge, Sn; $X, Y =$ S, Se, and Te) containing *T* and *H* phases have been explored using first-principles calculations and proposed for photocatalytic water splitting applications [24]. It has also been reported that the PbS_2 monolayer exhibits an unusual negative Poisson's ratio and suitable band edge alignment, which makes it a promising catalyst for photocatalytic water splitting applications [25]. Besides the family of group-IV chalcogenides, theoretical and experimental studies also concentrated on the other potentially stable compounds such as group IV–V monolayers [26–28]. A recent study extensively investigated the structural, vibrational, and electrical properties of two different phases of group IV–V crystals, including GeN, SnN, and PbN monolayers, and demonstrated that they are stable materials with semiconducting nature [29].

In line with the ongoing experimental and theoretical development of 2D materials for the realization of stable nanostructures, Hong *et al* have successfully synthesized a 2D septuple atomic layer of $MoSi_2N_4$ via chemical vapor deposition (CVD) technique [30]. They presented a novel approach for synthesizing new materials using an appropriate element (Si) to passivate the surface dangling bonds of MoN_2 during growth. The structure consists of a *1H*-MoN_2 monolayer sandwiched between two SiN surface layers. The $MoSi_2N_4$ crystal has been reported to be a wide bandgap non-magnetic semiconductor (1.94 eV) with high tensile strength and excellent ambient stability. The growth of $MoSi_2N_4$ monolayer led to the synthesis of WSi_2N_4 monolayer using the same approach [30]. Following the experimental progress, many similar 2D materials with a general formula of MA_2Z_4 (which *M*: Cr, Mo, W, V, Nb, Ta, Ti, Zr, Hf, Pd, Pt, *A*: Si or Ge and *Z*: N, P or As) have been predicted and characterized by *ab initio* methods [31–35]. Additionally, it has been found that depending on the atomic components, MA_2Z_4 monolayers exhibit diverse electronic and magnetic properties. For instance, unlike $MoSi_2N_4$ and WSi_2N_4 which are non-magnetic semiconductors [36], VSi_2N_4 [37] is a ferromagnetic semiconductor with a considerable valley polarization and the $TaSi_2N_4$ nanosheet is a metal and a type-I Ising

superconductor [38]. Recently, it has been reported that $MoSi_2N_4$ nanosheets containing single-metal atoms have intriguing properties that make them useful for heterogeneous catalysis applications [39]. Moreover, it has been shown that $MoSi_2N_4$ and WSi_2N_4 monolayers in contact to metal surfaces exhibit no Fermi level pinning and highly tunable Schottky barriers, which are promising features for application in microelectronics [40]. Using first-principles calculations, Mortazavi *et al* explored mechanical, electronic, piezoelectric properties, and lattice thermal conductivity of MA_2Z_4 ($M =$ Cr, Mo, W; $A =$ Si, Ge; $Z =$ N, P) monolayers in two different phases (i.e. the *T*-phase and the *H*-phase) [32]. In another study, Ding and Wang systematically investigated the structural stability and electronic properties of MSi_2N_4 monolayers with 4d and 5d TMs and identified 12 stable structures with *T*- or *H*-phase configurations [41]. So far, the investigations of the MA_2Z_4 family are mainly focused on the structures in which the core atom is a transition metal and a comprehensive study focusing on the alternative core atoms from post-transition elements has not been performed. With this in mind, in the present work, we study the structural, vibrational, mechanical, electronic, and optical properties of *1T*- and *1H*-MSi_2N_4 ($M =$ Ge, Sn, and Pb) monolayers by *ab initio* methods. The rest of the paper is organized as follows: detailed information about the computational methodology is described in section 2. In section 3, first, the ground state structures of the proposed materials are determined, and the corresponding structural parameters and cohesive energies are reported. Then their dynamical and thermal stabilities are investigated using phonon spectrum analysis and *ab initio* molecular dynamics (AIMD) simulations, respectively. Next, vibrational, mechanical, electronic, and optical properties of MSi_2N_4 monolayers are examined. Finally, we draw our conclusions in section 4.

2. Methodology

In the present study, all first principle calculations were carried out based on the density functional theory [42, 43] by using projector augmented wave (PAW) [44] pseudopotentials, as implemented in the Vienna *ab initio* simulation package (VASP) [45–48]. The Perdew–Burke–Ernzerhof (PBE) [49] functional of the generalized gradient approximation (GGA) was used to parameterize the exchange-correlation interactions. In addition, the Heyd–Scuseria–Ernzerhof (HSE06) [50, 51] functional was utilized to correct the underestimated electronic band gaps. The HSE06 functional was designed by mixing 25% of the exact Hartree–Fock (HF) exchange potential with 75% of PBE exchange and 100% of PBE correlation energy. For the expansion of the electronic wave function, a plane-wave basis set with a kinetic cutoff energy of

520 eV was taken, and a vacuum layer of $\sim$15 Å was inserted along the non-periodic direction to prevent the unrealistic interactions between the neighboring layers. The convergence value for electronic relaxation between the successive steps in the total energy calculations was less than 10^{-5} eV. In addition, during structural optimization (ionic positions and lattice constants), the maximum allowed force on each atom was less than 10^{-2} eV Å^{-1}, and the maximum pressure on the lattice was lowered to 1 kbar. The Gaussian smearing factor was taken to be 0.05 for the total energy calculations. Brillouin zone (BZ) integration was performed by a Γ-centered $16 \times 16 \times 1$ uniform k-point grid. To obtain the net charge transfer between the constituent atoms in the structures, the Bader technique was employed [52]. To check the lattice dynamic stability of the examined systems, the phonon band dispersions were calculated for $4 \times 4 \times 1$ supercells using a small-displacement approach as implemented in the PHONOPY [53] code. To analyze the thermal stability, *ab initio* molecular dynamics (AIMD) simulations were conducted by using a microcanonical ensemble method at constant temperatures (300 and 600 K) with a total simulation time of 10 ps and 1 fs time step. The finite displacement approach was used to calculate the vibrational frequencies and their corresponding off-resonant zone-centered Raman activity. For this purpose, at first, each atom in the primitive cell was displaced by ± 0.01 Å, and the corresponding dynamical matrix was generated. Subsequently, the vibrational modes were determined by direct diagonalization of the dynamical matrix. Following that, the Raman activity of each vibrational mode was computed by deriving the macroscopic dielectric tensor at the Γ point utilizing the small difference method [54]. A suitable Gaussian broadening was used to plot the Raman spectra based on the results acquired from the Raman calculations. In addition, the elastic constants were directly calculated using the density functional perturbation theory method with a sufficiently large k-point grid and cutoff energy of 700 eV. The linear response of a system is characterized by the complex dielectric function, $\varepsilon(\omega) = \varepsilon_1(\omega) + i\varepsilon_2(\omega)$, where the Kramers–Kronig relation was employed to obtain the real and imaginary components for optical calculations at the level of PBE and HSE functionals [55, 56].

3. Results and discussion

3.1. Structural properties

The geometry of the MSi$_2$N$_4$ (M = Ge, Sn, and Pb) monolayers is designed based on the structure of the synthesized 2D MoSi$_2$N$_4$ and WSi$_2$N$_4$ crystals. According to the geometrical structure of the MN$_2$ layer, two different lattices can be taken into account for each system, namely, $1T$ and $1H$ phases.

As illustrated in figure 1, in each form, MN$_2$ is sandwiched between two buckled honeycomb SiN layers. In both phases, the core atom (M) has six nearest N atoms, and depending on the arrangement of N atoms, either an octahedron ($1T$) or a triangular prism ($1H$) can be formed. The primitive cell of the examined systems is constructed from septuple atomic layers of N$-$Si$-$N$-M-$N$-$Si$-$N, which are held together with strong covalent bonding. The $1T$ and the $1H$ phases are both hexagonal lattices, their symmetries are D$_{3d}$ and D$_{3h}$, respectively, and their space groups belong to P$\bar{3}$m1 (No. 164) and P$\bar{6}$m2 (No. 187), respectively. The optimized structural parameters including in plane lattice constant ($\mathbf{a} = \mathbf{b}$), bond lengths between M-N (d_{M-N}) and Si-N atoms (d_{Si-N}), and the thickness ($\boldsymbol{h}$) of the nanosheets are listed in table 1. The calculated $\mathbf{a}$ of $1T$-GeSi$_2$N$_4$, $1T$-SnSi$_2$N$_4$, and $1T$-PbSi$_2$N$_4$ are 2.95, 3.05, and 3.12 Å, and $\mathbf{a}$ of $1H$-GeSi$_2$N$_4$, $1H$-SnSi$_2$N$_4$, and $1H$-PbSi$_2$N$_4$ are 2.93, 3.03, and 3.09, respectively. Notice that $\mathbf{a}$ of $1T$- and $1H$-MSi$_2$N$_4$ monolayers, slightly increases while going down the group IV elements (M atoms), which is correlated with increasing the atomic radius of core atoms. The bond length between M and N atoms (d_{M-N}) and the thickness of the crystals ($\boldsymbol{h}$) follows a similar trend as d_{M-N} elongates and $\boldsymbol{h}$ thickens with increasing the atomic radius of M atoms. In both phases, two types of Si-N bonds are formed in the inner and outer layers. The vertical bond between the Si atom and the inner N atom is shorter than the bond with the boundary N atom. Not surprisingly, the variation of bond lengths between Si and N atoms (d_{Si-N}) remains almost the same for all the systems. The charge partition analysis of the atoms in the framework of the Bader technique reveals that the number of electrons transferred from the M to surrounding N atoms are 2.00, 2.03, and 1.52 $|\mathbf{e}|$ in $1T$-GeSi$_2$N$_4$, $1T$-SnSi$_2$N$_4$, and $1T$-PbSi$_2$N$_4$, and 1.87, 1.92, and 1.45 $|\mathbf{e}|$, in $1H$-GeSi$_2$N$_4$, $1H$-SnSi$_2$N$_4$, and $1H$-PbSi$_2$N$_4$ monolayers, respectively. In both phases, the charge depletion from the Sn atoms to neighboring N atoms is highest, associated with the larger electronegativity difference between Sn and N atoms. This demonstrates that the bonding between N atoms and Sn possesses more ionic character than Ge and Pb. Furthermore, this reflects the general tendency of Pb to exhibit a more pronounced ionic character in its Pb(II) oxidation state when compared to Pb(IV). Although the variation of $\Delta\rho_{(M-N)}$ of $1T$- and $1H$-MSi$_2$N$_4$ structural phases with the same M atoms is not significant, the $\Delta\rho_{(M-N)}$ is slightly larger in $1T$ than $1H$ which is consistent with smaller d_{M-N} in $1T$ structures. The net charge transfer among the constituent atoms in the $1T$- and $1H$-MSi$_2$N$_4$ structures is illustrated in figure S1 of the supplemental material [57]. In addition, the planar averaged electrostatic potentials of the designed structures are computed, and their variations along the z axis are displayed in figure S2 of
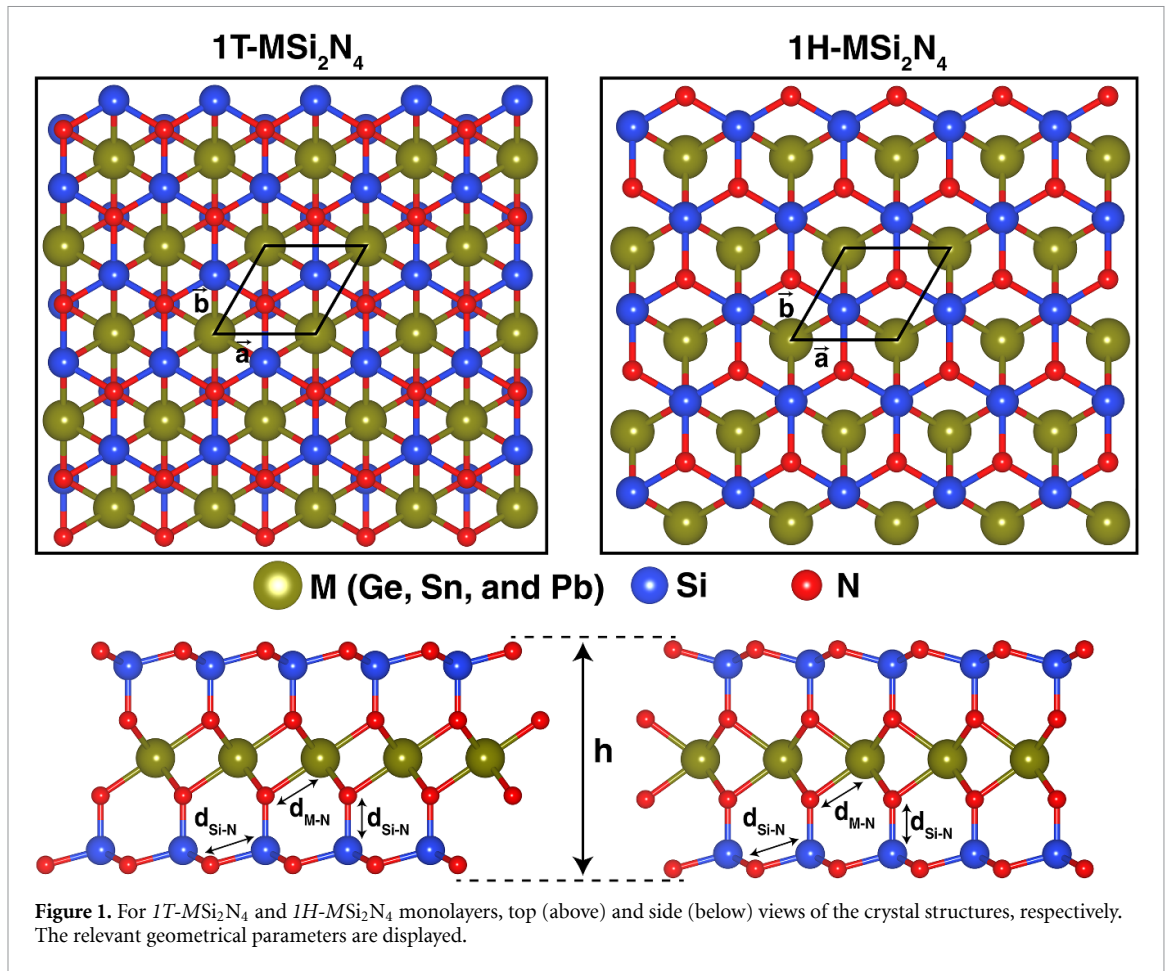
Figure 1. For *1T-M*Si$_2$N$_4$ and *1H-M*Si$_2$N$_4$ monolayers, top (above) and side (below) views of the crystal structures, respectively. The relevant geometrical parameters are displayed.

Table 1. The optimized lattice constants, a; atomic bond lengths, d$_{M-N}$ and d$_{Si-N}$; thickness, h; charge transfer from M to N, $\Delta\rho_{(M-N)}$; the calculated work function, Φ; cohesive energy per atom, E_C; the relaxed-ion elastic coefficients, C_{ij}; in-plane stiffness, Y_{2D}; Poisson's ratio, ν; ultimate tensile strain (UTS) for *1T-M*Si$_2$N$_4$ and *1H-M*Si$_2$N$_4$ (M = Ge, Sn, and Pb) monolayers.

Crystal structure	a (Å)	d$_{M-N}$ (Å)	d$_{Si-N}$ (Å)	(h) (Å)	$\Delta\rho_{(M-N)}$ (e$^-$)	Φ (eV)	E_C (eV/atom)	$C_{11}=C_{22}$ (N m^{-1})	C_{12} (N m^{-1})	Y_{2D} (N m^{-1})	ν (—)	UTS (%)
1*T*-GeSi$_2$N$_4$	2.95	2.00	1.75/1.77	6.62	2.00	6.11	5.41	484	124	452	0.25	18
1*T*-SnSi$_2$N$_4$	3.05	2.13	1.74/1.82	6.83	2.03	6.23	5.18	426	116	394	0.27	18
1*T*-PbSi$_2$N$_4$	3.12	2.23	1.73/1.85	7.01	1.52	5.73	4.72	361	108	328	0.30	16
1*H*-GeSi$_2$N$_4$	2.93	2.06	1.75/1.76	6.86	1.87	5.61	5.24	—	—	—	—	—
1*H*-SnSi$_2$N$_4$	3.03	2.16	1.74/1.81	6.99	1.92	6.23	5.09	448	136	406	0.30	16
1*H*-PbSi$_2$N$_4$	3.09	2.25	1.73/1.84	7.12	1.45	5.91	4.69	383	126	341	0.33	16

the supplemental material [57]. Generally, the work function of a material is defined as the energy difference between the vacuum-level potential and the Fermi energy of its surface ($\Phi = E_{\text{Vacuum}} - E_{\text{Fermi}}$). The work function is an intrinsic surface property of a material, and understanding and controlling its value is one of the fundamental factors in manipulating electron flow in various electronic applications. The computed results are listed in table 1, and they are found to be larger compared with the reported theoretical values for MoSi$_2$N$_4$ (5.12 eV) [58] and WSi$_2$N$_4$ (4.94) [59] monolayers. Following the structural optimization, to determine the strength of the binding between the constituent atoms in the

unit cell, the cohesive energy per atom (E_C) of the examined systems is calculated using the equation below:

$$E_C = \frac{[E_T(M) + 2E_T(\text{Si}) + 4E_T(\text{N})] - [E_T(M\text{Si}_2\text{N}_4)]}{7}$$

(1)

where $E_T(M)$, $E_T(\text{Si})$, and $E_T(\text{N})$ are the atomic energies of M, Si, and N atoms, respectively; $E_T(M\text{Si}_2\text{N}_4)$ corresponds to the total energy of the $M\text{Si}_2\text{N}_4$ nanosheets; and the denominator (7) is the numbers of the corresponding atoms in a primitive cell. The E_C of 1*T*- and 1*H*-MSi$_2$N$_4$ monolayers are in the range of 4.72–5.41 and 4.69–5.24 eV/atom, respectively. These
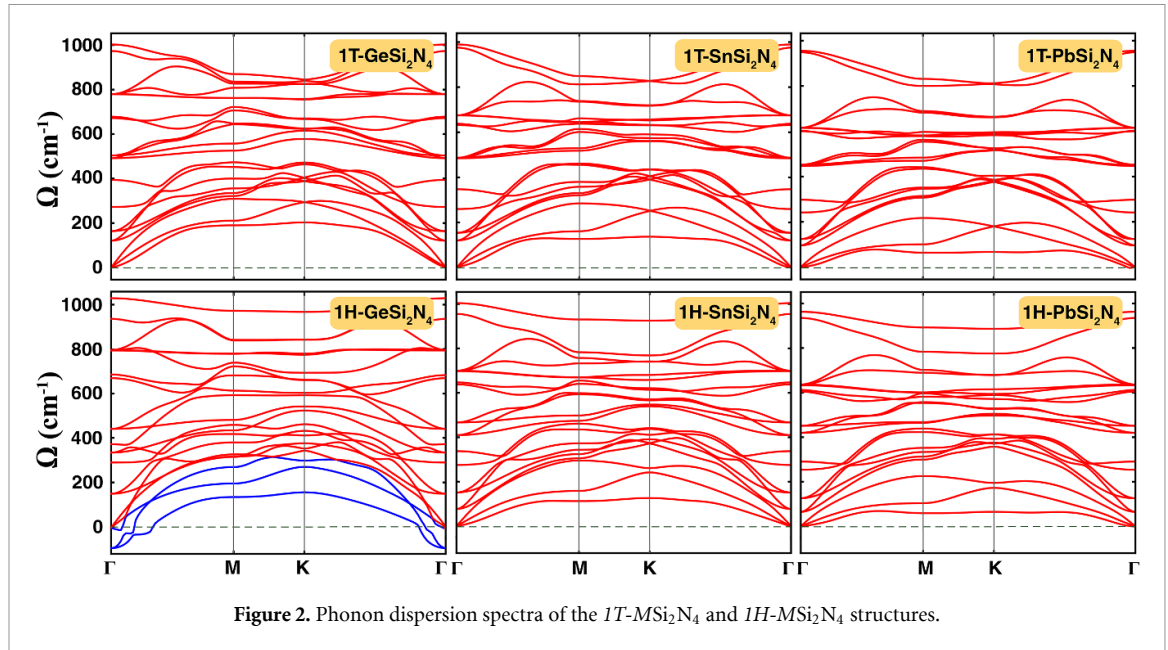
Figure 2. Phonon dispersion spectra of the *1T-M*Si$_2$N$_4$ and *1H-M*Si$_2$N$_4$ structures.

values are within the same range of reported values for PdSi$_2$N$_4$ (5.13 eV/atom) and PtSi$_2$N$_4$ (5.43 eV/atom) [35], implying strong binding energy between the constituent elements in the structures but smaller than MoSi$_2$N$_4$ monolayer (7.34 eV/atom) [60]. In accordance with the variation of **a** and the bond lengths between atoms, in both geometrical configurations, E_C gradually decreases when the atomic radii of the *M* element increase from Ge to Pb. As summarized in table 1, the 1*T*-phase compounds are energetically more favorable than their 1*H* counterparts (i.e. 1*T*-phases are more stable than 1*H*-phases). The E_C of GeSi$_2$N$_4$, SnSi$_2$N$_4$, and PbSi$_2$N$_4$ structures in 1*T*-phase are 0.17, 0.09, and 0.03 eV/atom higher than their 1*H* counterparts. As positive E_C solely is not sufficient to determine structural stability, additional analyses, such as phonon band dispersion and AIMD simulations, should be performed.

3.2. Dynamical stability

To examine the dynamical stability of designed crystals, *ab initio* phonon calculations at $T = 0$ are performed, and the corresponding phonon band spectra are represented in figure 2. In the analysis of phonon diagrams, whenever calculated dispersions of vibrational modes have a positive square of frequency ($\omega^2 > 0$) throughout the BZ, the material is regarded as dynamically stable. The existence of an imaginary frequency ($\omega^2 < 0$) corresponds to a non-restorative force, resulting in a reduction in potential energy as the atoms are displaced away from their equilibrium positions along a particular eigenmode. Except *1H-*GeSi$_2$N$_4$ monolayer, all phonon spectra of *1T-* and *1H-M*Si$_2$N$_4$ crystals are found to be free from any imaginary frequencies over the whole BZ, indicating the stability at low temperature. In the *1H-*GeSi$_2$N$_4$

system, unstable modes are correlated with a single degenerate acoustic mode and a double degenerate optical mode at the Γ-point of the BZ. The stable structures own similar phonon distributions, and all have twenty-one phonon branches in their phonon dispersions due to the presence of seven atoms in their primitive cells. In 2D ultrathin materials, there are three acoustic vibrational branches; the longitudinal acoustic mode (LA), the transverse acoustic mode (TA), and the out-of-plane flexural acoustic (ZA) branches. For the TA and LA branches, the frequency of acoustic phonon modes (ω) near the Γ point change linearly with phonon wave vector (q) (i.e. $\omega \propto q$), whereas ZA vibrational mode shows a parabolic dispersion ($\omega \propto q^2$) which is due to the fact that the force constants associated with the transverse vibrations of atoms decay rapidly [61]. It is seen that by increasing the weight of the *M* atom in both configurations, the highest vibrational frequency (ω_{max}) slightly decreases, and the overall frequency range of phonon modes gradually shrink. Generally, the compression of the phonon bands, particularly for the acoustic modes, brings about lower group velocity and stronger scattering, and, subsequently, lower thermal conductivity. Therefore, in both atomic configurations, due to the narrower dispersion of vibrational modes, PbSi$_2$N$_4$ monolayers possess smallest values of group velocities among the studied systems. To analyze the contribution of atoms to the phonon spectrum of examined systems, we performed the phonon density of states (PhDOS) calculations, and the obtained results are presented in figure S3, supplemental material [57]. For both phases, the low-frequency lattice vibrations (up to 200 cm^{-1}) are dominated by *M* atoms due to their heavier atomic masses. The partial DOS of Si ions in
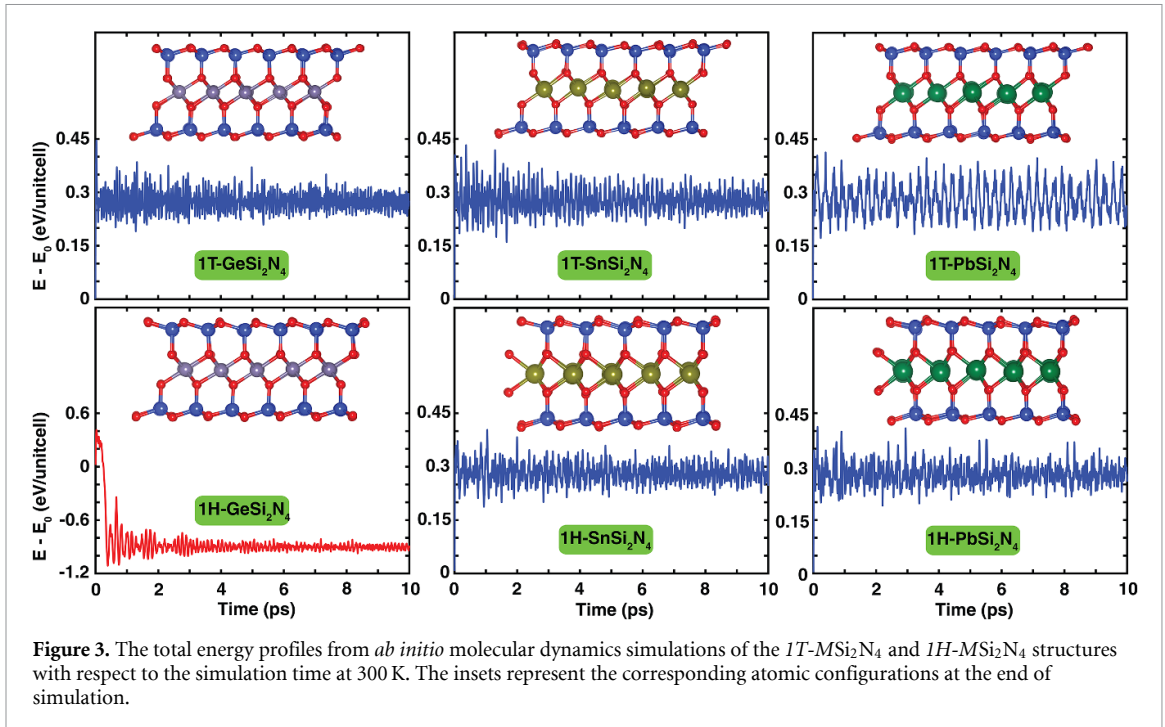
Figure 3. The total energy profiles from *ab initio* molecular dynamics simulations of the *1T-M*Si$_2$N$_4$ and *1H-M*Si$_2$N$_4$ structures with respect to the simulation time at 300 K. The insets represent the corresponding atomic configurations at the end of simulation.

the frequency range around 400 cm^{-1} has the same level as that of N atoms, while above that frequency, the high-frequency phonon modes are attributed to the vibrations of N atoms and, to a lesser extent, Si atoms.

Besides phonon band dispersion analysis, we perform AIMD simulation for *1T-* and *1H-M*Si$_2$N$_4$ crystals to examine their stability at elevated temperatures. Here, the structures are maintained at temperatures of 300 K and 600 K, and at ambient environment ($T = 300$ K and aqueous conditions). The simulations are performed for 10 ps. The size constraint of the unit cell is removed by taking a $4 \times 4 \times 1$ supercell for all studied nanosheets. The evolution of energy during the simulation and the final snapshots of the resulting geometries at 300 K, 600 K, and ambient environment are displayed in figures 3, S4, and S5, supplemental material [57], respectively. According to AIMD simulations, all examined systems except *1H-*GeSi$_2$N$_4$ monolayer are thermally stable. It is evident from the energy fluctuation graph and the final snapshot of the structure that *1H-*GeSi$_2$N$_4$ has a spontaneous phase transition (*1H* $\rightarrow$ *1T*). Additional investigations involving variation of temperature during AIMD simulations demonstrate that this transition occurs around $T = 30$–50 K. (see figure S6 supplemental material [57]). For the rest of the crystals, it appears that the gradient values of total energies of the systems fluctuate without any noticeable deviation during the whole simulation process, indicating the dynamical and thermal stability of *1T-* and *1H-M*Si$_2$N$_4$ monolayers at and above the room temperature. Thermal stability is crucial in various applications, such as thermoelectric devices, which often operate at high temperatures.

3.3. Vibrational properties

Raman spectroscopy is a strong tool for investigating and characterizing various nanomaterials, including 2D ultrathin crystals. The analysis and interpretation of experimental Raman data can be considerably simplified by comparison with the theoretically computed spectra. Vibrational properties and the corresponding Raman spectra are closely correlated with the geometry of the structures. Thus, their analysis can provide an insight into the physical properties associated with lattice symmetries. As mentioned above, the *1T-M*Si$_2$N$_4$ monolayers are characterized by the space group P$\bar{3}$m1 (D$_{3d}$) in the Hermann–Mauguin notation and the corresponding irreducible representation for vibrational modes in their spectrum can be represented by $\Gamma^{D_{3d}} = 3E_g + 3E_u + 3A_{1g} + 3A_{2u}$, where E_g and E_u phonon modes are attributed to the doubly degenerate symmetric and asymmetric in-plane vibrations, respectively, and the A_{1g} and A_{2u} modes represent the symmetric and asymmetric vibrations along the z axis, respectively. The E_g and A_{1g} are Raman active (RA) as they correspond to quadratic functions in the character table of D$_{3d}$, whereas E_u and A_{2u} are infrared active (IRA) modes. Thus, the investigated monolayers in *1T* phase should exhibit six peaks at their Raman spectrum. The calculated Raman activity of the *1T-M*Si$_2$N$_4$ nanosheets is depicted in figure 4(a), and the atomic displacements of each peak in the Raman spectra are labeled to identify the origins of Raman peaks. By going down the group IV elements in the nanosheets, the Raman spectra slightly shift toward lower frequencies, primarily due to the increased mass of *M* atoms. The most prominent RA peaks in the spectral profile of *1T-M*Si$_2$N$_4$ structures are the first and
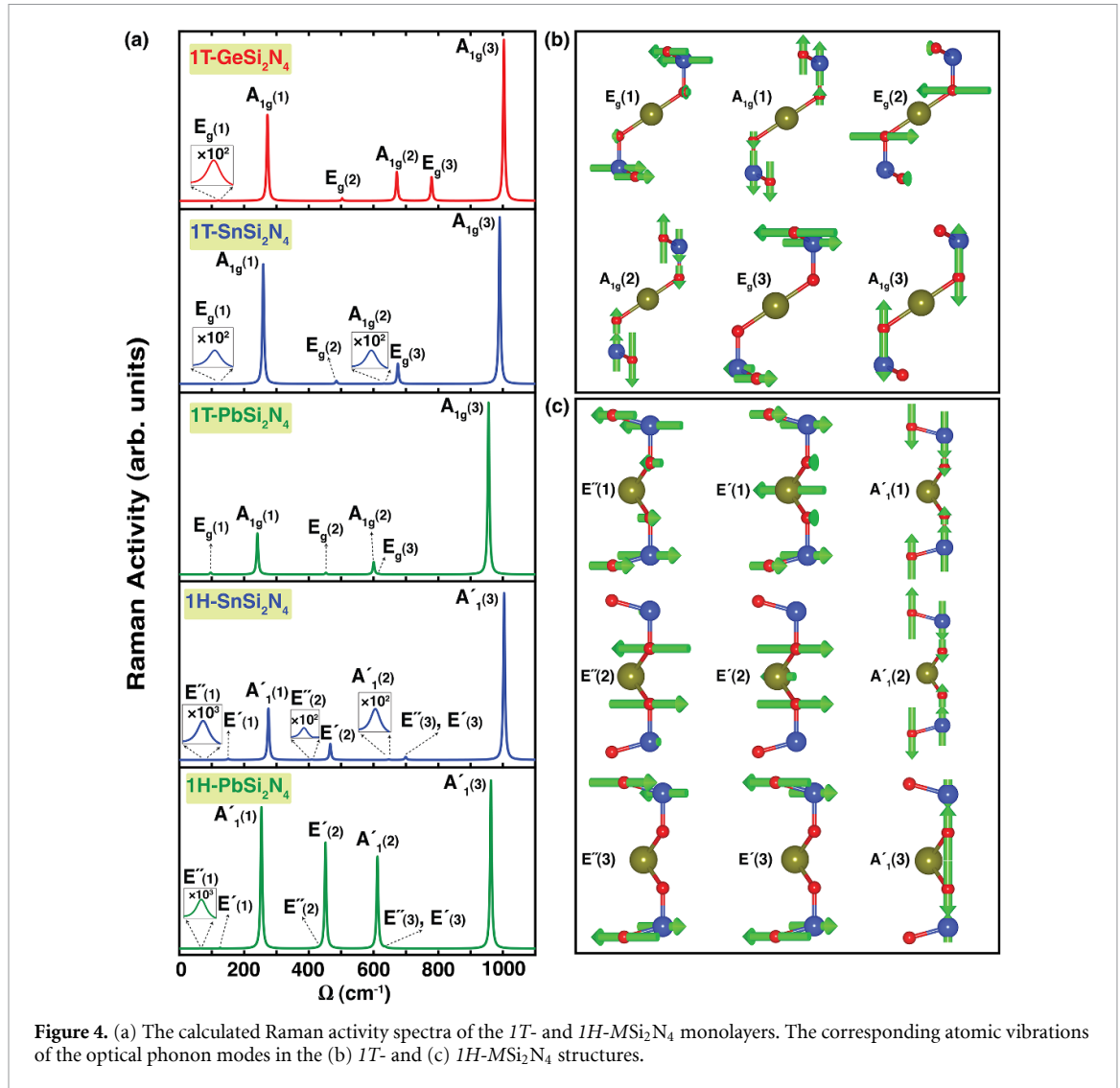
Figure 4. (a) The calculated Raman activity spectra of the *1T-* and *1H-M*Si$_2$N$_4$ monolayers. The corresponding atomic vibrations of the optical phonon modes in the (b) *1T-* and (c) *1H-M*Si$_2$N$_4$ structures.

third A_{1g} phonon mode [A_{1g} (1) and $A_{1g}(3)$]. The intensity of spectral peaks is determined by the contribution of macroscopic dielectric constants of corresponding vibrational modes to the Raman tensors. In figure 4(b), the RA atomic displacements (eigenvectors) of vibrational modes for *1T-M*Si$_2$N$_4$ are displayed. The first E_g and A_{1g} [$E_g(1)$ and A_{1g} (1)] phonon modes arise from the in-plane and out-of-plane vibration of buckled Si-N sublayers, respectively, while the inner N atoms have small contributions to the vibration. The $E_g(2)$ mode originates from the strong opposite in-plane vibration of inner N atoms in the unit cell, and the $A_{1g}(2)$ mode corresponds to symmetric out-of-plane vibrations of N-Si-N sub-layers against each other with respect to the M atoms. The $E_g(3)$ vibrational mode is attributed to the in-plane shear vibration of buckled Si-N sublayers. The $E_g(3)$ is followed by $A_{1g}(3)$ phonon modes which represent the symmetric out-of-plane vibration of Si and inner N pairs against each other, while the vibration of N atoms is more dominant. In the case of *1H* structures (which possess D$_{3h}$ symmetry), the group theory analysis shows that

the irreducible representation for the optical phonon modes at the Γ point can be assigned by $\Gamma^{D_{3h}} = 3E' + 3E'' + 3A_1' + 3A_2''$, in which the E' and E'' phonon modes are attributed to the doubly degenerate in-plane vibrations whereas A_1' and A_2'' modes correspond to the non-degenerate out-of-plane vibrations. Among the vibrational modes, A_2'' is IRA and the E', E'' and A_1' phonon modes are RA modes. This analysis reveals that the Raman spectrum of *1H-M*Si$_2$N$_4$ systems contains nine peaks. The calculated Raman spectrum of *1H*-SnSi$_2$N$_4$ and *1H*-PbSi$_2$N$_4$ monolayers are illustrated in figure 4(a). The most significant RA peaks for *1H*-SnSi$_2$N$_4$ monolayer are A_1' (1) and A_1' (3) vibrational modes which appear at 275 and 1003 cm^{-1}, respectively. Similar to *1H*-SnSi$_2$N$_4$, in *1H*-PbSi$_2$N$_4$ monolayer, the most intense peaks belong to the A_1' (1) and A_1' (3) phonon modes which are observed at 253 and 962 cm^{-1}, respectively. The next prominent peaks correspond to the E' (2), A_1' (2) vibrational modes, which appear at 451 and 612 cm^{-1}, respectively. To better explain the vibrational character of the *1H* structures, the atomic displacements (eigenvectors) of RA modes are displayed

in figure 4(c). Analysis of the most prominent peaks in the *1H* structures shows that the A_1' (1) phonon mode originates mainly from the symmetric out-of-plane vibration of the two N-Si-N sublayers with respect to the *M* atoms and the A_1' (3) vibrational mode arises from the symmetric vibration of Si and inner N atoms along *z* axis, while the vibration of N atoms is more dominant.
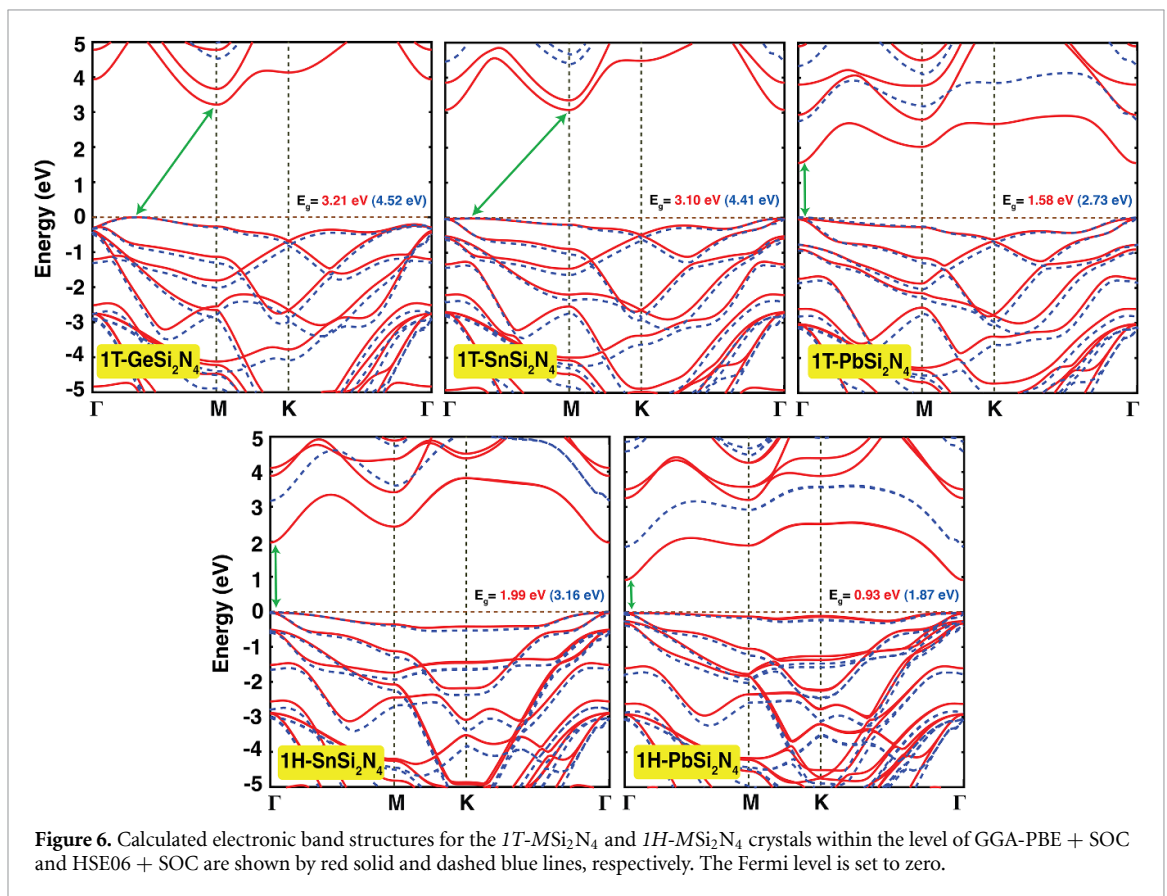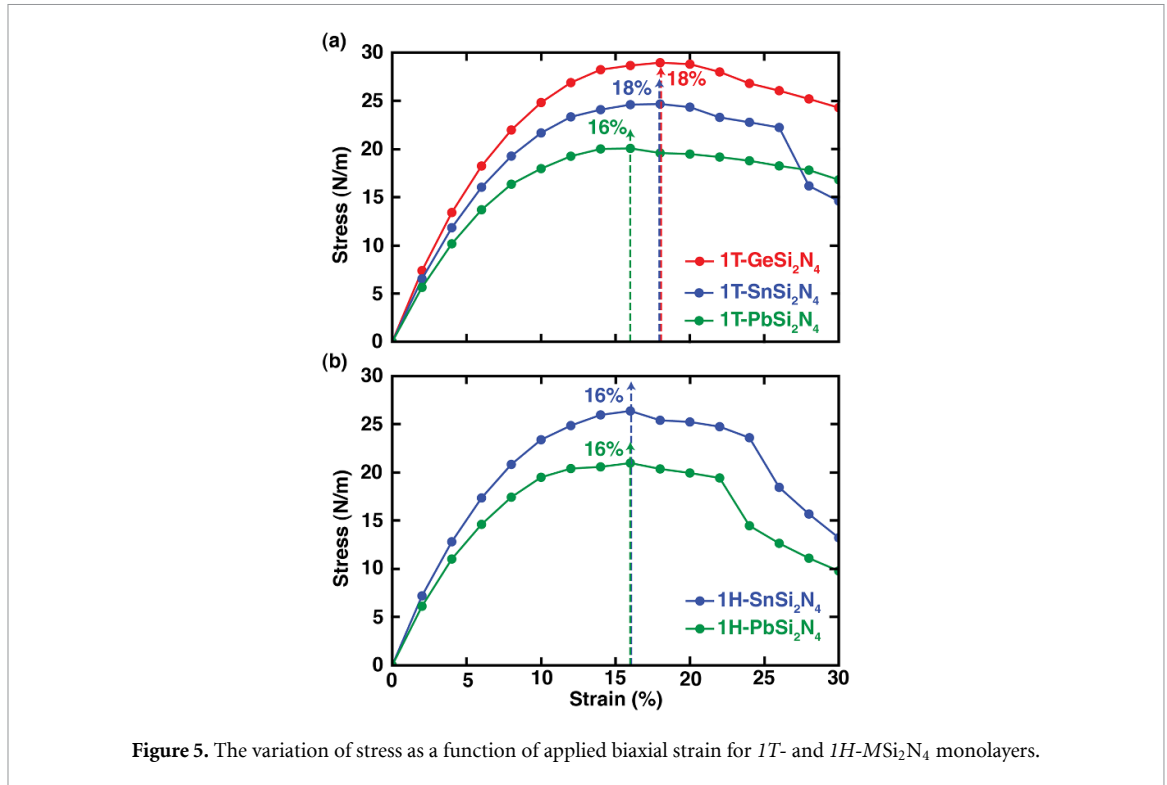
3.4. Mechanical properties

Next, we study the mechanical features of the stable structures in terms of in-plane stiffness (or 2D Young's modulus, Y_{2D}), Poisson's ratio (ν), and ultimate tensile strain (UTS). Mechanical properties, together with elastic stability, can be obtained by analyzing the elastic strain tensors (C_{ij}). Our calculated C_{ij}'s are listed in table 1. The elastic stability for the designed 2D hexagonal systems is ascertained when all C_{ij}'s are positive and satisfy the Born and Huang criteria [62, 63], i.e. [$C_{11} > |C_{12}|$ and $C_{66} = (C_{11} - C_{12})/2 > 0$]. From table 1, it can be found that the dynamically stable structures are also mechanically stable. In the 2D limit, Y_{2D} is defined as the measure of rigidity (or flexibility) of a crystal under the applied external load and can be calculated by the formula; $Y_{2D} = (C_{11}^2 - C_{12}^2)/C_{11}$. The calculated Y_{2D}'s are 452, 394, and 328 N m^{-1} for 1T-GeSi$_2$N$_4$, 1T-SnSi$_2$N$_4$, and 1T-PbSi$_2$N$_4$ monolayers, respectively, and the Y_{2D} of 1H-SnSi$_2$N$_4$ and 1H-PbSi$_2$N$_4$ are computed to be 406 and 341 N m^{-1}, respectively. Owing to the symmetric and isotropic crystal structure of the examined systems, the values of Y_{2D} along the *x* direction are identical to those along the *y* direction. When compared with the other members of MA_2Z_4 family, Y_{2D} is smaller than that of MoSi$_2$N$_4$ (491 N m^{-1}) [58] but larger than 1T- and 1H-YSi$_2$N$_4$ monolayers with 301, 236 N m^{-1} [41], respectively, indicating the rigidity of the proposed monolayers. In both phases, Y_{2D} decreases down the group of *M* atoms correlated to the reduction of E_C. Thus the smallest value is obtained for PbSi$_2$N$_4$. To clarify the role of applied stress on the mechanical features of the systems, we calculated the Poisson's ratio (ν) of the materials. ν is defined as the negative ratio of transverse contraction strain to longitudinal extension strain in the direction of the stretching force. Based on C_{ij}, ν is calculated by utilizing the relation; $\nu = C_{12}/C_{11}$ and the acquired results are in the range of 0.25–0.33 and are given in table 1. For comparison, the reported values of ν for MoSi$_2$N$_4$ and WSi$_2$N$_4$ crystals are found to be 0.28 and 0.27 [41], respectively. Different from Y_{2D}, ν increases with increasing the atomic mass of *M* atoms in the structures. According to the Christensen criterion, $\nu \approx 2/7$ proposed as a limit between ductile and brittle transition in 2D ultra-thin materials [64]. Thus, our calculated results indicate that 1T-GeSi$_2$N$_4$ and 1T-SnSi$_2$N$_4$ monolayers are brittle with $\nu < 2/7$ which is associated with the more ionic nature of *M*-N bonding in the structures, and 1T-PbSi$_2$N$_4$ and

both stable *1H* crystals with higher values of 2/7 possess a ductile character. We further examine the UTS, which is another important intrinsic mechanical feature of 2D materials. UTS is defined as the maximum value of tensile strains that a material can withstand without breaking. Generally, strain is present in experiments, whether intrinsically or intentionally, and during the process of strain engineering, extreme strains can be applied to the 2D materials. Therefore, a suitable material for strain-coupled applications of 2D materials should retain its integrity, even at high levels of induced strain. To estimate UTS of the systems, we employed a $3 \times 3 \times 1$ supercell to restrict the artificial effects of small unit cell size and then measured the amount of stress imposed into the system upon various biaxial tensile strains. The stress–strain curve of stable *1T*- and *1H*-MSi$_2$N$_4$ structures is depicted in figures 5(a) and (b), respectively. The figure shows that the stress–strain curve appears linear for all monolayers up to $\sim 8\%$, specifying the systems' elastic regime. Beyond the elastic limit, the examined systems undergo plastic deformation, and stress gradually increases until reaching the maximum point. Our results indicate that the UTS of the studied systems is in the range of 16–18 %, which is comparable with that of ultimate strain for MoSi$_2$N$_4$ (19.5%) [65] monolayer. It can be seen that *1T*- and *1H*-MSi$_2$N$_4$ nanosheets exhibit prominent mechanical features such as sizeable in-plane stiffness and high UTS that make them promising candidates for elastic energy storage applications. In addition, the piezoelectric properties of the proposed crystals have been calculated, and the acquired results are presented in the supplemental materials [57]. These findings are subsequently compared with other members of the *MSi$_2$N$_4$* family [66].

3.5. Electronic properties

We further investigated the electronic properties of the *1T*- and *1H*-MSi$_2$N$_4$ nanosheets. The electronic band structure, the atomic contributions to the electronic band dispersions in *1T* and *1H* forms, and partial density of states (PDOS) of dynamically stable systems are shown in figures 6 and S7–S9, supplemental material [57], respectively. At first, electronic band structures are computed at the level of GGA-PBE (E_g^{PBE}). Then, the SOC effect is included with the GGA functional ($E_g^{\text{PBE-SOC}}$) to analyze the band splitting near the energy band gap. The obtained results are summarized in table 2. It can be seen that all structures are wide band gap semiconductors, and except for *1T*-GeSi$_2$N$_4$ and *1T*-SnSi$_2$N$_4$ nanosheets, they have direct band gaps. In both phases, by increasing the atomic radius of *M* atoms, $E_g^{\text{PBE-SOC}}$ narrows, which is caused by the reduced orbital overlap in the suggested systems. In addition, according to the acquired results, the *1T* structures possess wider $E_g^{\text{PBE-SOC}}$ than the corresponding *1H* counterparts. As seen, there are no significant effects of

Figure 5. The variation of stress as a function of applied biaxial strain for *1T*- and *1H*-*M*Si₂N₄ monolayers.

Figure 6. Calculated electronic band structures for the *1T*-*M*Si₂N₄ and *1H*-*M*Si₂N₄ crystals within the level of GGA-PBE + SOC and HSE06 + SOC are shown by red solid and dashed blue lines, respectively. The Fermi level is set to zero.

SOC on the band structure of the designed crystals, which is due to the presence of light elements such as N and Si in the systems and the existence of inversion symmetry in *1T* structures. Given that weak SOC leads to long-lasting spin coherence, this can open up new perspectives for these materials in spintronics. When the calculations are repeated using the hybrid functionals with the inclusion of SOC ($E_g^{\text{HSE-SOC}}$), similar trends with wider band gaps are obtained; however, the band structure profiles are not

Table 2. For *1T*- and *1H*-MSi$_2$N$_4$ ($M =$ Ge, Sn, and Pb) monolayers, energy band gaps at the level of GGA-PBE, E_g^{PBE}; GGA-PBE + SOC, $E_g^{\text{PBE-SOC}}$; HSE06 + SOC, $E_g^{\text{HSE-SOC}}$; and the locations of VBM and CBM edges in the BZ.
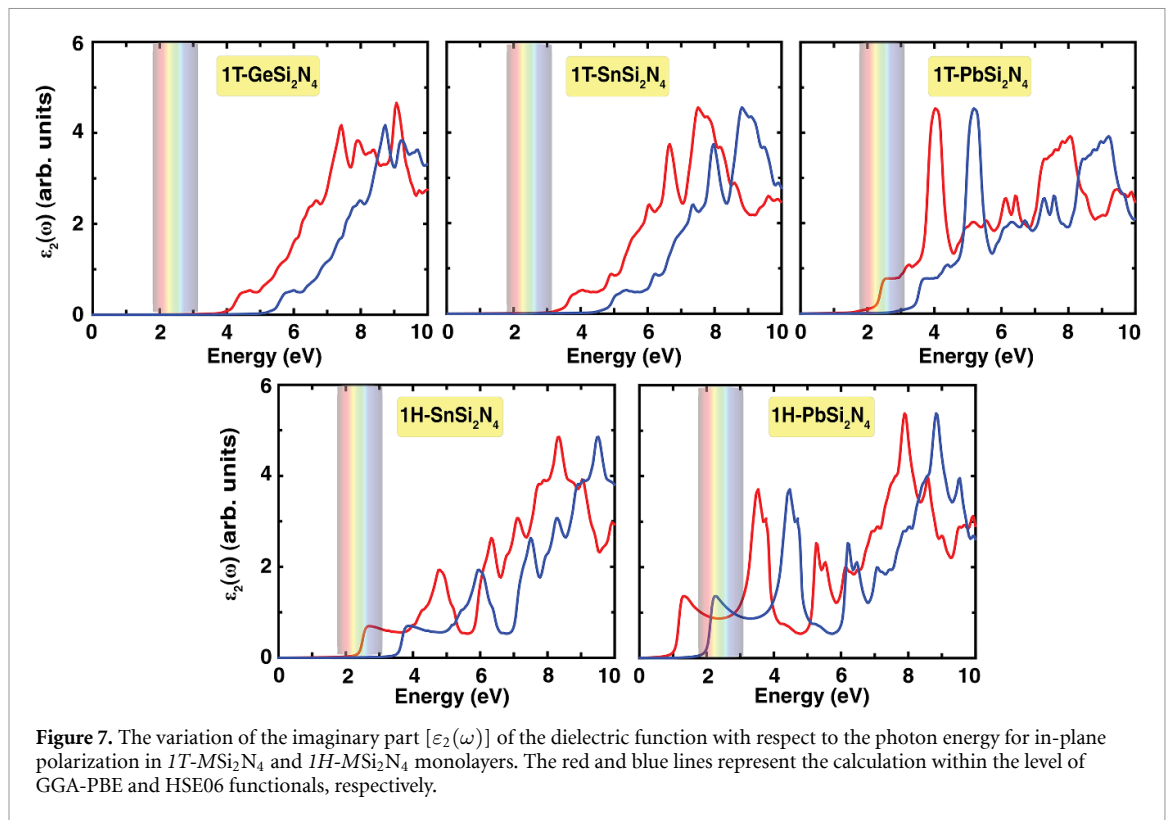
Structure	E_g^{PBE} (eV)	$E_g^{\text{PBE-SOC}}$ (eV)	$E_g^{\text{HSE-SOC}}$ (eV)	VBM/CBM (—)
1T-GeSi$_2$N$_4$	3.21	3.21	4.52	Γ-M/M
1T-SnSi$_2$N$_4$	3.11	3.10	4.41	Γ-M/M
1T-PbSi$_2$N$_4$	1.59	1.58	2.73	Γ/Γ
1H-SnSi$_2$N$_4$	2.00	1.99	3.16	Γ/Γ
1H-PbSi$_2$N$_4$	0.93	0.93	1.87	Γ/Γ

changed. The $E_g^{\text{HSE-SOC}}$ of 1*T*-GeSi$_2$N$_4$, 1*T*-SnSi$_2$N$_4$, and 1*T*-PbSi$_2$N$_4$ nanosheets are calculated to be 4.52, 4.41, and 2.73 eV, respectively, and for 1*H*-SnSi$_2$N$_4$, and 1*H*-PbSi$_2$N$_4$ monolayers, $E_g^{\text{HSE-SOC}}$ are found to be 3.16 and 1.87 eV, respectively. Accordingly, the proposed structures can be considered wide-band-gap semiconductors whose energy band gap covers a range from ultraviolet to the visible light parts of the optical spectrum. Recent studies have shown that 2D wide-band-gap materials are desirable for a variety of applications such as solar cells, photoelectrochemical catalysts, and field effect transistors (FET) [67, 68]. In addition, a flat valence band can be observed in the structures, which indicates that the holes as charge carriers in the systems have low mobility. This flatness is more noticeable in 1*H*-SnSi$_2$N$_4$ and 1*H*-PbSi$_2$N$_4$ monolayers. Analysis of atom-resolved projection of electronic band structure shows that in all monolayers, N atoms are the main contributors to the highest valence band (HVB). In the lowest conduction band (LCB), the dominance of N states diminishes, and a mixture of states from all atomic species can be found, especially around the conduction band minimum (CBM). Therefore, due to the dominance of N atoms in both HVB and LCB of all examined nanosheets, we further explored the orbital decomposed band structures projected onto p-orbitals of N atoms. There is a consistent pattern among all crystals that the HVB consists primarily of p_y and p_z orbitals, and p_x orbitals are only present around the degenerate Γ-point of the HVB, except for 1*H*-PbSi$_2$N$_4$ where the degeneracy at the Γ-point is lifted, and no significant contribution for p_x orbitals can be found. On the other hand, the LCBs of the examined systems are mainly attributed to the moderate contribution of the N-p orbitals, and the main contribution to the CBM arises from the p_x of the N atoms. Moreover, the analysis of PDOS results demonstrated that in 1*T*- and 1*H*-MSi$_2$N$_4$ monolayers, the valence band maximum (VBM) are mainly derived from p orbitals of N atoms.

3.6. Optical properties

Finally, the in-plane optical response of the stable 1*T*- and 1*H*-MSi$_2$N$_4$ structures is analyzed. The invest-

igation of a material's optical properties is a useful tool in envisioning its potential industrial applications. The optical properties can be determined from the frequency-dependent complex dielectric function, $\varepsilon(\omega)$, which can be formulated as [$\varepsilon(\omega) = \varepsilon_1(\omega) + i\varepsilon_2(\omega)$]. Calculating $\varepsilon_2(\omega)$ of the dielectric function enables us to determine various optical properties, such as absorbance and absorption coefficient. The variation of $\varepsilon_2(\omega)$ as a function of photon energy for in-plane light polarization of the designed systems calculated within PBE and HSE06 functionals is presented in figure 7. According to the figure, HSE06 optical band gaps for both 1*T* and 1*H* nanosheets are notably larger than those obtained from PBE calculations. Due to the geometrical symmetry of the hexagonal lattice along the *x*- and *y*- directions, the optical spectra in the considered systems are found to be isotropic. Analysis of the HSE06 results reveals that for 1*T*-GeSi$_2$N$_4$, 1*T*-SnSi$_2$N$_4$, and 1*T*-PbSi$_2$N$_4$ monolayers, the first prominent optical peaks are noticed at $\approx$5.7, 5 and 3.6 eV (UV region), respectively, while for 1*H*-SnSi$_2$N$_4$ and 1*H*-PbSi$_2$N$_4$ crystal structures, the onset of optical absorption emerges in the near ultraviolet and visible light (3.79 and 2.22 eV) region of the optical spectrum, respectively, in accordance with their direct electronic band gap. The first absorption peak of MoSi$_2$N$_4$ monolayer is calculated at 2.31 eV, which is in the visible range of the optical spectrum [58]. According to the calculated imaginary part of the dielectric function, the first prominent peak point corresponds to the transition from the valence band to the conduction band states. Therefore, the aforementioned values are attributed to the fundamental bandgap of proposed nanostructures. In both phases, the absorption peak positions for the suggested crystals move toward lower energy (redshifts) by increasing the atomic mass of the core element. The main peak region of absorption for 1*T*- and 1*H*-PbSi$_2$N$_4$ monolayers appears around 4–5 eV. Our results show that the suggested 2D systems are wide-bandgap semiconductors with intense optical peaks within the ultraviolet and visible spectral region, making them promising materials for various optoelectronic applications such as solar energy utilization and UV detectors.

Figure 7. The variation of the imaginary part $[\varepsilon_2(\omega)]$ of the dielectric function with respect to the photon energy for in-plane polarization in *1T-M*Si$_2$N$_4$ and *1H-M*Si$_2$N$_4$ monolayers. The red and blue lines represent the calculation within the level of GGA-PBE and HSE06 functionals, respectively.

4. Conclusion

In conclusion, inspired by the theoretical and experimental studies on 2D MA_2Z_4 family, the stability and fundamental properties of *1T*- and *1H-M*Si$_2$N$_4$ (M = Ge, Sn, and Pb) monolayers are investigated via *ab initio* calculations. Our results reveal that both phases have similar cohesive energies, however, it has been found that the *1T* structures are more energetically favorable than their *1H* counterparts. The stability analyses performed by phonon dispersion calculations and AIMD simulations, reveal that except *1H*-GeSi$_2$N$_4$ monolayer, which is dynamically and thermally unstable, the other designed nanosheets are stable at and above ambient temperature. Our vibrational analysis reveals that the *1T-M*Si$_2$N$_4$ monolayers possess six Raman peaks in their spectrum whereas *1H-M*Si$_2$N$_4$ structures reveals nine characteristic RA mode. It is also found that the distinctive peaks of the same structural phases have similar frequencies and intensities. The elastic stability and mechanical features of the designed nanosheets are explored by calculating their elastic constants (C_{ij}), in-plane stiffness (Y_{2D}), Poisson's ratio (ν), and UTS and they are found to be isotropic. The calculated Y_{2D} values for stable monolayers range from 328 to 452 N m^{-1}, indicating their rigidity, and the estimated values of UTS lie between 16%–18% which are comparable to the reported values of MoSi$_2$N$_4$ and WSi$_2$N$_4$ monolayers. The electronic structure investigation shows all suggested crystals are wide band gap semiconductors with energy band gaps ranging from

1.87 to 4.52 eV at the level of HSE06+SOC which spans a range from visible light to the UV region of the optical spectrum. Lastly, the analysis of optical properties shows that the designed systems have isotropic optical spectra, and depending on the type of the system, high absorption of ultraviolet and visible light (particularly in *1H*-PbSi$_2$N$_4$ monolayer) is predicted. Our results provide a comprehensive overview concerning the fundamental physical properties of *1T*- and *1H-M*Si$_2$N$_4$ (M = Ge, Sn, and Pb) semiconductors and highlight their intriguing properties and suggests them as promising candidates for diverse nanomechanical and optoelectronics applications.

Data availability statement

All data that support the findings of this study are included within the article (and any supplementary files).

Acknowledgments

Conflict of interest

The authors declare no competing interests.

ORCID iDs

Biplab Sanyal ⬥ https://orcid.org/0000-0002-3687-4223
Sergio Tosoni ⬥ https://orcid.org/0000-0001-5700-4086

References

[1] Novoselov K S, Geim A K, Morozov S V, Jiang D-E, Zhang Y, Dubonos S V, Grigorieva I V and Firsov A A 2004 Electric field effect in atomically thin carbon films *Science* **306** 666–9

[2] Tan C *et al* 2017 Recent advances in ultrathin two-dimensional nanomaterials *Chem. Rev.* **117** 6225–331

[3] Butler S Z *et al* 2013 Progress, challenges and opportunities in two-dimensional materials beyond graphene *ACS Nano* **7** 2898–926

[4] Miró P, Audiffred M and Heine T 2014 An atlas of two-dimensional materials *Chem. Soc. Rev.* **43** 6537–54

[5] Vogt P, De Padova P, Quaresima C, Avila J, Frantzeskakis E, Asensio M C, Resta A, Ealet B and Le Lay G 2012 Silicene: compelling experimental evidence for graphenelike two-dimensional silicon *Phys. Rev. Lett.* **108** 155501

[6] Liu C-C, Feng W and Yao Y 2011 Quantum spin Hall effect in silicene and two-dimensional germanium *Phys. Rev. Lett.* **107** 076802

[7] Tao L, Cinquanta E, Chiappe D, Grazianetti C, Fanciulli M, Dubey M, Molle A and Akinwande D 2015 Silicene field-effect transistors operating at room temperature *Nat. Nanotechnol.* **10** 227–31

[8] Zhang W, Huang J-K, Chen C-H, Chang Y-H, Cheng Y-J and Li L-J 2013 High-gain phototransistors based on a CVD MoS$_2$ monolayer *Adv. Mater.* **25** 3456–61

[9] Mak K F, Lee C, Hone J, Shan J and Heinz T F 2010 Atomically thin MoS$_2$: a new direct-gap semiconductor *Phys. Rev. Lett.* **105** 136805

[10] Wu F, Huang C, Wu H, Lee C, Deng K, Kan E and Jena P 2015 Atomically thin transition-metal dinitrides: high-temperature ferromagnetism and half-metallicity *Nano Lett.* **15** 8277–81

[11] Manzeli S, Ovchinnikov D, Pasquier D, Yazyev O V and Kis A 2017 2D transition metal dichalcogenides *Nat. Rev. Mater.* **2** 1–15

[12] Ataca C, Sahin H and Ciraci S 2012 Stable, single-layer MX$_2$ transition-metal oxides and dichalcogenides in a honeycomb-like structure *J. Phys. Chem.* C **116** 8983–99

[13] Wang Q H, Kalantar-Zadeh K, Kis A, Coleman J N and Strano M S 2012 Electronics and optoelectronics of two-dimensional transition metal dichalcogenides *Nat. Nanotechnol.* **7** 699–712

[14] Qian Z, Jiao L and Xie L 2020 Phase engineering of two-dimensional transition metal dichalcogenides *Chin. J. Chem.* **38** 753–60

[15] Chen C, Ji X, Xu K, Zhang B, Miao L and Jiang J 2017 Prediction of T- and H- phase two-dimensional transition-metal carbides/nitrides and their semiconducting–metallic phase transition *ChemPhysChem* **18** 1897–902

[16] Song S, Keum D H, Cho S, Perello D, Kim Y and Lee Y H 2016 Room temperature semiconductor–metal transition of MoTe$_2$ thin films engineered by strain *Nano Lett.* **16** 188–93

[17] Thakur D, Kumar P and Balakrishnan V 2020 Phase selective CVD growth and photoinduced 1T → 1H phase transition in a WS$_2$ monolayer *J. Mater. Chem.* C **8** 10438–47

[18] Burton L A, Colombara D, Abellon R D, Grozema F C, Peter L M, Savenije T J, Dennler G and Walsh A 2013 Synthesis, characterization and electronic structure of single-crystal SnS, Sn$_2$S$_3$ and SnS$_2$ *Chem. Mater.* **25** 4908–16

[19] Zhang X, Cui Y, Sun L, Li M, Du J and Huang Y 2019 Stabilities and electronic and piezoelectric properties of two-dimensional tin dichalcogenide derived Janus monolayers *J. Mater. Chem.* C **7** 13203–10

[20] Hu Z, Ding Y, Hu X, Zhou W, Yu X and Zhang S 2019 Recent progress in 2D group IV–IV monochalcogenides: synthesis, properties and applications *Nanotechnology* **30** 252001

[21] Varjovi M J, Ershadrad S and Sanyal B 2023 Structural, vibrational, elastic, electronic and piezoelectric properties of binary γ–GeX and ternary γ–Ge$_2$XX′ monolayers (X, X′ = S, Se and Te) *Phys. Rev.* B **107** 195421

[22] Xu L *et al* 2019 Large-scale growth and field-effect transistors electrical engineering of atomic-layer SnS$_2$ *Small* **15** 1904116

[23] Bacaksiz C, Cahangirov S, Rubio A, Senger R T, Peeters F M and Sahin H 2016 Bilayer SnS$_2$: tunable stacking sequence by charging and loading pressure *Phys. Rev.* B **93** 125403

[24] Xie M, Shang Y, Li X, Da Y and Liu X 2023 An *ab initio* study of two dimensional SnX$_2$ and Janus SnXY (X = S, Se) nanosheets as potential photocatalysts for water splitting *ACS Appl. Nano Mater.* **6** 10569–80

[25] Jin W, Pang J, Yue L, Xie M, Kuang X and Lu C 2022 Multifunctional PbS$_2$ monolayer with an in-plane negative Poisson ratio and photocatalytic water splitting properties *J. Phys. Chem. Lett.* **13** 10494–9

[26] Barreteau C, Michon B, Besnard C and Giannini E 2016 High-pressure melt growth and transport properties of SiP, SiAs, GeP and GeAs 2D layered semiconductors *J. Cryst. Growth* **443** 75–80

[27] Huang B, Zhuang H L, Yoon M, Sumpter B G and Wei S-H 2015 Highly stable two-dimensional silicon phosphides: different stoichiometries and exotic electronic properties *Phys. Rev.* B **91** 121401

[28] Ashton M, Sinnott S B and Hennig R G 2016 Computational discovery and characterization of polymorphic two-dimensional IV–V materials *Appl. Phys. Lett.* **109** 192103

[29] Özdamar B, Özbal G, Çınar M N, Sevim K, Kurt G, Kaya B and Sevinçli H 2018 Structural, vibrational and electronic properties of single-layer hexagonal crystals of group IV and V elements *Phys. Rev.* B **98** 045431

[30] Hong Y-L *et al* 2020 Chemical vapor deposition of layered two-dimensional MoSi$_2$N$_4$ materials *Science* **369** 670–4

[31] Novoselov K S 2020 Discovery of 2D van der Waals layered MoSi$_2$N$_4$ family *Natl Sci. Rev.* **7** 1842–4

[32] Mortazavi B, Javvaji B, Shojaei F, Rabczuk T, Shapeev A V and Zhuang X 2021 Exceptional piezoelectricity, high thermal conductivity and stiffness and promising photocatalysis in two-dimensional MoSi$_2$N$_4$ family confirmed by first-principles *Nano Energy* **82** 105716

[33] Yin Y, Gong Q, Yi M and Guo W 2023 Emerging versatile two-dimensional MoSi$_2$N$_4$ family *Adv. Funct. Mater.* **33** 2214050

[34] Yao H, Zhang C, Wang Q, Li J, Yu Y, Xu F, Wang B and Wei Y 2021 Novel two-dimensional layered MoSi$_2$Z$_4$ (Z = P, As): new promising optoelectronic materials *Nanomaterials* **11** 559

[35] Varjovi M J, Kilic M E and Durgun E 2023 First-principles investigation on the structural, vibrational, mechanical, electronic and optical properties of MSi$_2$Z$_4$ (M: Pd and Pt, Z: N and P) monolayers *Phys. Rev. Mater.* **7** 034002

[36] Zeng J, Xu L, Luo X, Chen T, Tang S-H, Huang X and Wang L-L 2021 Z-scheme systems of ASi$_2$N$_4$ (A = Mo or W) for photocatalytic water splitting and nanogenerators *Tungsten* **4** 52–59

[37] Cui Q, Zhu Y, Liang J, Cui P and Yang H 2021 Spin-valley coupling in a two-dimensional VSi$_2$N$_4$ monolayer *Phys. Rev. B* **103** 085421

[38] Wang L *et al* 2021 Intercalated architecture of MA$_2$Z$_4$ family layered van der Waals materials with emerging topological, magnetic and superconducting properties *Nat. Commun.* **12** 2361

[39] He M, Chen X, Zhou Y, Xu C, Li X, Luo Q and Yang J 2023 A first-principles study of regulating spin states of MoSi$_2$N$_4$ supported single-atom catalysts via doping strategy for enhancing electrochemical nitrogen fixation activity *J. Phys. Chem. Lett.* **14** 7100–7

[40] Wang Q *et al* 2021 Efficient ohmic contacts and built-in atomic sublayer protection in MoSi$_2$N$_4$ and WSi$_2$N$_4$ monolayers *npj 2D Mater. Appl.* **5** 71

[41] Ding Y and Wang Y 2021 Computational exploration of stable 4d/5d transition-metal MSi$_2$N$_4$ (M = Y–Cd and Hf–Hg) nanosheets and their versatile electronic and magnetic properties *J. Phys. Chem. C* **125** 19580–91

[42] Kohn W and Sham L J 1965 Self-consistent equations including exchange and correlation effects *Phys. Rev.* **140** A1133

[43] Hohenberg P and Kohn W 1964 Inhomogeneous electron gas *Phys. Rev.* **136** B864

[44] Blöchl P E 1994 Projector augmented-wave method *Phys. Rev. B* **50** 17953

[45] Kresse G and Hafner J 1993 *Ab initio* molecular dynamics for liquid metals *Phys. Rev. B* **47** 558

[46] Kresse G and Hafner J 1994 *Ab initio* molecular-dynamics simulation of the liquid-metal–amorphous-semiconductor transition in germanium *Phys. Rev. B* **49** 14251

[47] Kresse G and Furthmüller J 1996 Efficiency of *ab-initio* total energy calculations for metals and semiconductors using a plane-wave basis set *Comput. Mater. Sci.* **6** 15–50

[48] Kresse G and Furthmüller J 1996 Efficient iterative schemes for *ab initio* total-energy calculations using a plane-wave basis set *Phys. Rev. B* **54** 11169

[49] Perdew J P, Burke K and Ernzerhof M 1996 Generalized gradient approximation made simple *Phys. Rev. Lett.* **77** 3865

[50] Heyd J, Scuseria G E and Ernzerhof M 2003 Hybrid functionals based on a screened Coulomb potential *J. Chem. Phys.* **118** 8207–15

[51] Krukau A V, Vydrov O A, Izmaylov A F and Scuseria G E 2006 Influence of the exchange screening parameter on the performance of screened hybrid functionals *J. Chem. Phys.* **125** 224106

[52] Henkelman G, Arnaldsson A and Jónsson H 2006 A fast and robust algorithm for bader decomposition of charge density *Comput. Mater. Sci.* **36** 354–60

[53] Togo A and Tanaka I 2015 First principles phonon calculations in materials science *Scr. Mater.* **108** 1–5

[54] Fonari A and Stauffer S 2013 *vasp-raman.py* (available at: https://github.com/raman-sc/VASP/)

[55] Cudazzo P, Tokatly I V and Rubio A 2011 Dielectric screening in two-dimensional insulators: implications for excitonic and impurity states in graphane *Phys. Rev. B* **84** 085406

[56] Berkelbach T C, Hybertsen M S and Reichman D R 2013 Theory of neutral and charged excitons in monolayer transition metal dichalcogenides *Phys. Rev. B* **88** 045318

[57] See supplemental material for additional details on Bader charge analyses, planar average of the electrostatic potential diagrams, *ab initio* molecular dynamics results at 600 K, AIMD simulations at ambient conditions, Energy vs temperature in AIMD run, the atomic contributions to the electronic band dispersions in 1T and 1H phases, and orbital projected density of states (PDOS) results, for the *M*Si$_2$Z$_4$ monolayers

[58] Bafekry A, Faraji M, Hoat D, Shahrokhi M, Fadlallah M, Shojaei F, Feghhi S, Ghergherehchi M and Gogova D 2021 MoSi$_2$N$_4$ single-layer: a novel two-dimensional material with outstanding mechanical, thermal, electronic and optical properties *J. Phys. D: Appl. Phys* **54** 155303

[59] Ma X, Bo H, Gong X, Yuan G, Peng Z, Lu J and Xie Q 2023 Tunable Schottky barrier of WSi$_2$N$_4$/graphene heterostructure via interface distance and external electric field *Appl. Surf. Sci.* **615** 156385

[60] Alavi-Rad H 2022 Strain engineering in optoelectronic properties of MoSi$_2$N$_4$ monolayer: ultrahigh tunability *Semicond. Sci. Technol.* **37** 065018

[61] Liu F, Ming P and Li J 2007 *Ab initio* calculation of ideal strength and phonon instability of graphene under tension *Phys. Rev. B* **76** 064120

[62] Born M and Huang K 1954 *Dynamical Theory of Crystal Lattices* (Clarendon)

[63] Mouhat F and Coudert F-X 2014 Necessary and sufficient elastic stability conditions in various crystal systems *Phys. Rev. B* **90** 224104

[64] Christensen R M 2020 Mechanisms and measures for the ductility of materials failure *Proc. R. Soc. A* **476** 20190719

[65] Li Q, Zhou W, Wan X and Zhou J 2021 Strain effects on monolayer MoSi$_2$N$_4$: ideal strength and failure mechanism *Physica E* **131** 114753

[66] Wang X, Ju W, Wang D, Li X and Wan J 2023 Flexible MA$_2$Z$_4$ (M = Mo, W; A = Si, Ge and Z = N, P, As) monolayers with outstanding mechanical, dynamical, piezoelectric properties and anomalous dynamic polarization *Phys. Chem. Chem. Phys.* **25** 18247–58

[67] Lu Y and Warner J H 2020 Synthesis and applications of wide bandgap 2D layered semiconductors reaching the green and blue wavelengths *ACS Appl. Electron. Mater.* **2** 1777–814

[68] Odobel F and Pellegrin Y 2013 Recent advances in the sensitization of wide-band-gap nanostructured p-type semiconductors. Photovoltaic and photocatalytic applications *J. Phys. Chem. Lett.* **4** 2551–64